Journal of Sound and Vibration 346 (2015) 216–228

Contents lists available at ScienceDirect

Journal of Sound and Vibration

journal homepage: www.elsevier.com/locate/jsvi

Mechanisms of sound amplification and sound reduction in the flapping flight of side-by-side airfoils

A. Manela *, M. Halachmi

Faculty of Aerospace Engineering, Technion - Israel Institute of Technology, Haifa 32000, Israel

ARTICLE INFO

Article history:
Received 7 September 2014
Received in revised form
9 February 2015
Accepted 16 February 2015
Handling Editor: D. Juve
Available online 17 March 2015

ABSTRACT

The acoustic signature of side-by-side airfoils, subject to small-amplitude harmonic pitching and incoming flow unsteadiness, is investigated. The two-dimensional near-field problem is formulated using thin-airfoil theory, where flow unsteadiness is modeled as a passing line vortex, and wake evolution is calculated via the Brown and Michael formula. Assuming that the setup is acoustically compact, acoustic radiation is obtained by means of the Powell–Howe acoustic analogy. The associated compact Green's function is calculated numerically using potential-flow analysis of the fluid–structure flow domain. Results, comparing the acoustic radiation of the double-airfoil system to a reference case of a single airfoil, point to several mechanisms of sound attenuation and sound amplification, caused by airfoil–airfoil and airfoils-wake interactions. It is found that counter-phase pitching of the airfoils results in effective cloaking of the system, which otherwise becomes significantly noisy (as a 5/2-power of the pitching frequency) at large frequencies. In addition, depending on the distance between airfoils, in-phase pitching may result in an acoustic signature equivalent to a single airfoil (when the airfoils are adjacent) or to two separate airfoils (when the airfoils are far apart). In general, flow unsteadiness produces more sound when interacting with a double (compared with a single) airfoil setup. However, airfoils' nonlinear wake–wake interactions give rise to a sound reduction mechanism, which becomes most efficient at times when incoming vorticity passes above airfoils' leading and trailing edges. The present scheme can be readily extended to consider the acoustic properties of various double-airfoil configurations, as well as multiple (>2) airfoil setups.

1. Introduction

Multi-body fluid–structure interactions have been a topic of increasing interest in the past few decades. Motivated by ubiquitous everyday phenomena in natural and engineering applications, studies have initially focused on the canonical problem of flow interference between two circular cylinders [1]. Later works on the near-field dynamics of multi-body interactions have considered other geometrical configurations, taking account, in each of the problem studied, of the combined effects of multi-body interactions with associated flow fields. Among several setups studied, multi-airfoil configurations have received particular attention, owing to their relevance for analyzing formation locomotion in fish and birds and gaining insight into the aerodynamic advantages of group flight (e.g., [2–6]).

* Corresponding author.
E-mail address: amanela@technion.ac.il (A. Manela).

http://dx.doi.org/10.1016/j.jsv.2015.02.032
0022-460X/

Investigations on far-field acoustic radiation from multi-body setups have received relatively less attention. Nevertheless, while current efforts focus mainly on sound scattering from single-body geometries [7], an increasing number of works have recently appeared, studying noise emission phenomena in multi-structure setups. Towards this end, Inoue et al. [8] and Doolan [9] considered sound emission from a double cylinder array, focusing on the role of cylinders separation distance and associated vortex shedding on the radiated sound. Several other workers have carried out acoustic investigations of multi-body setups containing airfoils. Thus, Casalino et al. [10] predicted the noise produced by rod–airfoil interactions using the Ffowcs–Williams–Hawkings acoustic analogy. Leclercq and Doolan [11] investigated the sound generated by the interaction between a blade and a block. Winkler and Carolus [12] and Gruber et al. [13] suggested means for reducing tandem airfoil noise through active blowing or additional trailing and leading edge serrations, respectively. While these and other studies have revealed some of the consequences between near-field and far-field flow characteristics in multi-structure configurations, considerable work still remains to investigate the complex phenomena of sound emission in multi-airfoil systems.

The purpose of the present work is to study in detail the far-field vibroacoustic signature of a basic two-dimensional double-airfoil setup. The study builds upon previous analyses of the vibroacoustic signature of single-airfoil configurations, where the effects of leading edge forcing, structure elasticity, and flow unsteadiness on system near- and far-field behaviors have been investigated (see Refs. [14–16] and works cited therein). Practically, the present investigation may be of interest as a starting point for analyzing the acoustic signature of multi-airfoil interaction. A side-by-side thin-airfoil configuration is considered as a model problem, and high-Reynolds low-Mach flow conditions are assumed. To mimic flapping-flight state and include unsteady flow effects, small-amplitude pitching actuation is introduced, together with incoming flow non-uniformity in the form of a passing line vortex. Extending on the above-mentioned single-airfoil investigations, the formulation of the near-field problem couples the effect of leading edge actuation to the fluid–structure interaction problem in a nonlinear description. Assuming that the setup is acoustically compact, the far-field calculation is carried out via application of the Powell–Howe analogy. The results obtained present several mechanisms by which sound suppression and sound amplification phenomena occur in the double-airfoil system considered.

The paper is organized as follows. In Section 2, both near- and far-field problems are introduced and analyzed. In Section 3, results are presented and discussed for the separate cases of pitching airfoils for steady flow; non-pitching airfoils for unsteady flow; and the combined setup of animated airfoils for unsteady conditions. Concluding remarks are given in Section 4, and a technical description of the numerical calculation of the compact Green's function, used for obtaining the far-field radiation, is relegated to an Appendix.

2. Problem formulation

2.1. Near-field aerodynamics

Fig. 1 presents a schematic of the near-field problem. Consider a two-dimensional setup of two identical, flat, and infinitely thin rigid airfoils, of chord $2a$. The airfoils are nominally placed parallel to the x_1-direction in a "side-by-side" setup, with a separation distance of $2s$ between their leading edges in the x_2-direction. The system is subject to low-Mach uniform flow of magnitude U in the x_1-direction. At time $t \geq 0$, an incident line vortex of strength Γ is released into the flow at a prescribed location and interacts with the system. Simultaneously, harmonic pitching actuation, with common amplitude $\bar{\varepsilon}$ (where an overbar denotes a non-dimensional quantity) and frequency ω, is applied at both airfoils' leading edges:

$$\alpha_{LE}^{u} = \bar{\varepsilon}\sin(\omega t) \quad \text{and} \quad \alpha_{LE}^{l} = \bar{\varepsilon}\sin(\omega t + \phi). \tag{1}$$

In (1), α_{LE} denotes the angle between instantaneous airfoil's positions and their unperturbed states, and superscripts "u" and "l" mark hereafter quantities corresponding to "upper" (nominally at $x_2 = s$) and "lower" (nominally at $x_2 = -s$) airfoils. The phase shift between pitching actuations is denoted by ϕ, and it is assumed that pitching amplitude, $\bar{\varepsilon}$, and incident vortex strength, Γ, are sufficiently small, so that linearized thin-airfoil theory can be applied. Given the small angles of

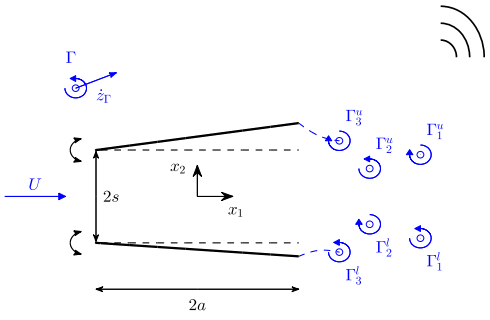

Fig. 1. Schematic of the side-by-side airfoil setup.

attack considered, leading edge flow detachment is excluded, and fluid vorticity is allowed only at the incident vortex location and along a trailing edge wake. In addition, the small mean-flow Mach number assumed allows us to treat the near-field flow as incompressible and potential.

We formulate an initial value problem, where at $t=0$ the airfoils are aligned with the x_1-axis, the incident vortex Γ is set into the flow, and leading edge actuation is commenced. The initial vortex location is chosen sufficiently upstream of the airfoil, to approximate a case where the vortex initially has a negligible effect on system near-field dynamics. Adopting complex-variable notation, we denote the instantaneous vortex location and velocity by $z_\Gamma(t)=x_{1_\Gamma}(t)+\mathrm{i}x_{2_\Gamma}(t)$ and $\dot{z}_\Gamma(t)=\dot{x}_{1_\Gamma}(t)+\mathrm{i}\dot{x}_{2_\Gamma}(t)$, respectively.

In accordance with potential thin-airfoil theory, trailing edge singularity is induced by incident vortex and airfoil motion interactions with surrounding fluid, and reflects through square root divergence of the fluid velocity field. This singularity is regularized by application of the unsteady Kutta condition, and results in release of vorticity at the airfoil trailing edge. Production of trailing edge vorticity is modeled via the Brown and Michael equation [17,18], a commonly used scheme to approximate high Reynolds number vortex shedding from two-dimensional sharp ends. The scheme has been applied in studies on both near-field dynamics [19–21] and sound emission [22,23] problems. The model assumes the trailing edge wake to be a discrete sequence of concentrated line vortices whose position and strength vary with time. At a given time, one vortex is being shed from the airfoil trailing edge, in the form of a thin connecting sheet of infinitesimal circulation ending in a concentrated core of finite circulation. The core strength changes with time according to the Kutta condition, while its position is governed by the Brown and Michael formula. When the time derivative of vortex strength changes sign, the vortex is detached from the thin sheet and propagates as a "free" line vortex with "frozen" (fixed) circulation; the shedding of the next vortex is then initiated.

Applying thin-airfoil methodology, each of the upper and lower airfoils is represented by distribution of circulation, $\gamma_a^u(x_1,t)$ and $\gamma_a^l(x_1,t)$, respectively, per unit length. To specify these distributions, no-penetration conditions are imposed on the structures. Based on the form of pitching actuation (1), airfoils' deflections in the x_2 direction, ξ^u and ξ^l, are given by

$$\xi^u(x_1,t)=\bar{\varepsilon}(x_1+a)\sin(\omega t)+s \text{ and } \xi^l(x_1,t)=\bar{\varepsilon}(x_1+a)\sin(\omega t+\phi)-s, \tag{2}$$

where $-a\le x_1\le a$. Accordingly, the form of no-penetration condition is

$$\frac{\partial\xi^u}{\partial t}+U\frac{\partial\xi^u}{\partial x_1} = \mathrm{Im}\left\{\frac{\mathrm{i}}{2\pi}\left[\fint_{-a}^{a}\frac{\gamma_a^u(p,t)\,\mathrm{d}p}{x_1-p}+\int_{-a}^{a}\frac{\gamma_a^l(p,t)\,\mathrm{d}p}{x_1-p+2\mathrm{i}s}+\frac{\Gamma}{z^u-z_\Gamma}+\sum_{k=1}^{n^u}\frac{\Gamma_k^u}{z^u-z_{\Gamma_k^u}}+\sum_{k=1}^{n^l}\frac{\Gamma_k^l}{z^u-z_{\Gamma_k^l}}\right]\right\}, \tag{3}$$

for the upper airfoil, and

$$\frac{\partial\xi^l}{\partial t}+U\frac{\partial\xi^l}{\partial x_1} = \mathrm{Im}\left\{\frac{\mathrm{i}}{2\pi}\left[\int_{-a}^{a}\frac{\gamma_a^u(p,t)\,\mathrm{d}p}{x_1-p-2\mathrm{i}s}+\fint_{-a}^{a}\frac{\gamma_a^l(p,t)\,\mathrm{d}p}{x_1-p}+\frac{\Gamma}{z^l-z_\Gamma}+\sum_{k=1}^{n^u}\frac{\Gamma_k^u}{z^l-z_{\Gamma_k^u}}+\sum_{k=1}^{n^l}\frac{\Gamma_k^l}{z^l-z_{\Gamma_k^l}}\right]\right\}, \tag{4}$$

for the lower airfoil. In (3) and (4), $z^u=x_1+\mathrm{i}s$ and $z^l=x_1-\mathrm{i}s$ mark locations along the upper and lower airfoils, respectively, and $z_{\Gamma_k^u}$ and $z_{\Gamma_k^l}$ denote instantaneous locations of k th trailing edge vortices originating from the upper and lower airfoils, respectively. Barred integrals mark Cauchy principal value integrals, to be evaluated based on Glauert integral method [24]. Summations in Eqs. (3) and (4) are carried out over all n^u and n^l wake vortices contained in the upper and lower airfoil wakes.

The incident and trailing edge vortex dynamics are governed by their equations of motion. The motion of the incident vortex Γ is governed by

$$\frac{\mathrm{d}z_\Gamma}{\mathrm{d}t}=W_\Gamma^*, \tag{5}$$

where an asterisk marks the complex conjugate of a complex number, and

$$W_\Gamma=U-\frac{\mathrm{i}}{2\pi}\left(\int_{-a}^{a}\frac{\gamma_a^u(x_1,t)\,\mathrm{d}x_1}{z_\Gamma-z^u}+\int_{-a}^{a}\frac{\gamma_a^l(x_1,t)\,\mathrm{d}x_1}{z_\Gamma-z^l}+\sum_{k=1}^{n^u}\frac{\Gamma_k^u}{z_\Gamma-z_{\Gamma_k^u}}+\sum_{k=1}^{n^l}\frac{\Gamma_k^l}{z_\Gamma-z_{\Gamma_k^l}}\right) \tag{6}$$

is the conjugate velocity induced at the instantaneous vortex location, after removing its self-singularity. Similarly, motions of the $\Gamma_1^u,\ldots,\Gamma_{n^u-1}^u,\Gamma_1^l,\ldots,\Gamma_{n^l-1}^l$ "frozen" trailing edge vortices are governed by

$$\frac{\mathrm{d}z_{\Gamma_k^u}}{\mathrm{d}t}=W_{\Gamma_k^u}^* \quad \text{and} \quad \frac{\mathrm{d}z_{\Gamma_k^l}}{\mathrm{d}t}=W_{\Gamma_k^l}^* \tag{7}$$

for the upper and lower airfoil wake vortices, respectively, where

$$W_{\Gamma_k^u}=U-\frac{\mathrm{i}}{2\pi}\left(\int_{-a}^{a}\frac{\gamma_a^u(x_1,t)\,\mathrm{d}x_1}{z_{\Gamma_k^u}-z^u}+\int_{-a}^{a}\frac{\gamma_a^l(x_1,t)\,\mathrm{d}x_1}{z_{\Gamma_k^u}-z^l}+\sum_{\substack{m=1\\ m\neq k}}^{n^u}\frac{\Gamma_m^u}{z_{\Gamma_k^u}-z_{\Gamma_m^u}}+\sum_{m=1}^{n^l}\frac{\Gamma_m^l}{z_{\Gamma_k^u}-z_{\Gamma_m^l}}+\frac{\Gamma}{z_{\Gamma_k^u}-z_\Gamma}\right),$$

$$W_{\Gamma_k^l} = U - \frac{\mathrm{i}}{2\pi}\left(\int_{-a}^{a}\frac{\gamma_a^u(x_1,t)\,\mathrm{d}x_1}{z_{\Gamma_k^l}-z^u}+\int_{-a}^{a}\frac{\gamma_a^l(x_1,t)\,\mathrm{d}x_1}{z_{\Gamma_k^l}-z^l}+\sum_{m=1}^{n^u}\frac{\Gamma_m^u}{z_{\Gamma_k^l}-z_{\Gamma_m^u}}+\sum_{\substack{m=1\\m\neq k}}^{n^l}\frac{\Gamma_m^l}{z_{\Gamma_k^l}-z_{\Gamma_m^l}}+\frac{\Gamma}{z_{\Gamma_k^l}-z_\Gamma}\right). \tag{8}$$

In line with the discussion of the Brown and Michael theory, the time-varying strengths and positions of the instantaneously shed n^u and n^l trailing edge vortices are governed by the Brown and Michael equations[1]:

$$\frac{\mathrm{d}z_{\Gamma_{n^u}^u}}{\mathrm{d}t}+\left(z_{\Gamma_{n^u}^u}-z_{\mathrm{TE}}^u\right)\frac{1}{\Gamma_{n^u}^u}\frac{\mathrm{d}\Gamma_{n^u}^u}{\mathrm{d}t}=W^*_{\Gamma_{n^u}^u}\quad\text{and}\quad\frac{\mathrm{d}z_{\Gamma_{n^l}^l}}{\mathrm{d}t}+\left(z_{\Gamma_{n^l}^l}-z_{\mathrm{TE}}^l\right)\frac{1}{\Gamma_{n^l}^l}\frac{\mathrm{d}\Gamma_{n^l}^l}{\mathrm{d}t}=W^*_{\Gamma_{n^l}^l}, \tag{9}$$

where $W^*_{\Gamma_{n^u}^u}$ and $W^*_{\Gamma_{n^l}^l}$ are given by Eq. (8) with $k=n^u$ and $k=n^l$, respectively, and z_{TE}^u and z_{TE}^l mark the complex-variable locations of airfoil's trailing edges. The strength of the shed vortices is specified by Kelvin's theorem

$$\Gamma_{n^u}^u(t)=-\int_{-a}^{a}\gamma_a^u(x_1,t)\,\mathrm{d}x_1-\sum_{k=1}^{n^u-1}\Gamma_k^u\quad\text{and}\quad\Gamma_{n^l}^l(t)=-\int_{-a}^{a}\gamma_a^l(x_1,t)\,\mathrm{d}x_1-\sum_{k=1}^{n^l-1}\Gamma_k^l, \tag{10}$$

ensuring that the sum of total circulation of each airfoil and its wake circulation vanishes at all times.

The nonlinear system of Eqs. (2)–(10) is solved in conjunction with an initial condition for the vortex location,

$$z_\Gamma(t=0)=z_{\Gamma_0}, \tag{11}$$

and imposition of the unsteady Kutta condition,

$$\gamma_a^u(a,t)=\gamma_a^l(a,t)=0, \tag{12}$$

requiring that the fluid velocity at each trailing edge is finite. We assume that release of the first trailing edge vortex at each airfoil starts at $t=0$; the system evolution is then followed for $t>0$ via numerical integration. Details regarding problem scaling and numerical analysis are given in Section 2.3.

2.2. Far-field acoustic radiation

Considering the present small-amplitude-actuation, low-Mach, and high-Reynolds-number flow setup, the far-field ($|\mathbf{x}|\to\infty$) acoustic pressure is governed by the Powell–Howe acoustic analogy [7,27]:

$$\left(\frac{1}{c_0^2}\frac{\partial^2}{\partial t^2}-\nabla^2\right)p=\rho_0\frac{\partial^2\xi^u}{\partial t^2}\delta(x_2-s)+\rho_0\frac{\partial^2\xi^l}{\partial t^2}\delta(x_2+s)+\rho_0\nabla\cdot(\boldsymbol{\Omega}\times\mathbf{V}), \tag{13}$$

where c_0 is the speed of sound, δ is the Dirac delta function, $\mathbf{V}$ is the fluid velocity, and $\boldsymbol{\Omega}$ is the vector of fluid vorticity. The latter is given by the sum of

$$\boldsymbol{\Omega}_\Gamma=\hat{\boldsymbol{x}}_3\Gamma\delta(\mathbf{x}-\mathbf{x}_\Gamma(t))\ \text{and}$$
$$\boldsymbol{\Omega}_w=\sum_{k=1}^{n^u}\boldsymbol{\Omega}_{\Gamma_k^u}+\sum_{k=1}^{n^l}\boldsymbol{\Omega}_{\Gamma_k^l}=\hat{\boldsymbol{x}}_3\left(\sum_{k=1}^{n^u}\Gamma_k^u\delta(\mathbf{x}-\mathbf{x}_{\Gamma_k^u}(t))+\sum_{k=1}^{n^l}\Gamma_k^l\delta(\mathbf{x}-\mathbf{x}_{\Gamma_k^l}(t))\right), \tag{14}$$

which mark the incident and trailing edge wake vorticities, respectively. In (14), $\mathbf{x}=(x_1,x_2)$ marks a point in the plane of flow, and $\hat{\boldsymbol{x}}_3$ marks a unit vector in the normal-to-plane direction. Combining Eqs. (13) and (14), the acoustic pressure is decomposed into a sum of "airfoil motion", "incident vortex" and "wake" contributions:

$$p(\mathbf{x},t)=p_\xi(\mathbf{x},t)+p_\Gamma(\mathbf{x},t)+p_w(\mathbf{x},t), \tag{15}$$

where

$$p_\xi(\mathbf{x},t)=p_\xi^u(\mathbf{x},t)+p_\xi^l(\mathbf{x},t)$$
$$=\rho_0\frac{\partial}{\partial t}\left[\int_0^\infty\left(\frac{\partial\xi^u}{\partial\tau}\oint_{S^u}G(\mathbf{x},\mathbf{y},t-\tau)\,\mathrm{d}S(\mathbf{y})+\frac{\partial\xi^l}{\partial\tau}\oint_{S^l}G(\mathbf{x},\mathbf{y},t-\tau)\mathrm{d}S(\mathbf{y})\right)\mathrm{d}\tau\right], \tag{16}$$

$$p_\Gamma(\mathbf{x},t)=-\rho_0\int_0^\infty\int_{\mathcal{V}_\Gamma}(\boldsymbol{\Omega}_\Gamma\times\mathbf{V}_\Gamma)\cdot\frac{\partial G}{\partial\mathbf{y}}(\mathbf{x},\mathbf{y},t-\tau)\,\mathrm{d}\mathbf{y}\,\mathrm{d}\tau, \tag{17}$$

[1] Corrections to the original Brown and Michael formula have been suggested during the years, to account for a spurious dipole induced by the time dependence of circulation of the shed vortex [25,26]. Yet, since these corrections are limited to stationary-structure setups, and as recent studies have indicated the minor effect of using a corrected Brown and Michael formula on the calculated sound in a finite-chord airfoil setup (e.g., [15]), we expect that no qualitative effects should occur due to present use of the original equation.

and

$$p_w(\mathbf{x},t)=p_w^u(\mathbf{x},t)+p_w^l(\mathbf{x},t)=-\rho_0\int_0^\infty\left(\sum_{k=1}^{n^u}\int_{\mathcal{V}_{\Gamma_k^u}}\left(\mathbf{\Omega}_{\Gamma_k^u}\times\mathbf{V}_{\Gamma_k^u}\right)\cdot\frac{\partial G}{\partial\mathbf{y}}(\mathbf{x},\mathbf{y},t-\tau)\,\mathrm{d}\mathbf{y}\right.$$
$$\left.+\sum_{k=1}^{n^l}\int_{\mathcal{V}_{\Gamma_k^l}}\left(\mathbf{\Omega}_{\Gamma_k^l}\times\mathbf{V}_{\Gamma_k^l}\right)\cdot\frac{\partial G}{\partial\mathbf{y}}(\mathbf{x},\mathbf{y},t-\tau)\,\mathrm{d}\mathbf{y}\right)\mathrm{d}\tau. \tag{18}$$

In (16)–(18), $\mathcal{S}^u$ and $\mathcal{S}^l$ are the upper and lower airfoil surfaces, respectively; $\mathcal{V}_\Gamma$, $\mathcal{V}_{\Gamma_k^u}$ and $\mathcal{V}_{\Gamma_k^l}$ denote the fluid regions occupied by the incident and trailing edge vortices; $G(\mathbf{x},\mathbf{y},t-\tau)$ is the acoustic Green's function having a vanishing normal derivative on the undisturbed airfoils; and $\mathbf{V}_\Gamma$, $\mathbf{V}_{\Gamma_k^u}$ and $\mathbf{V}_{\Gamma_k^l}$ are the velocities of incident and trailing edge vortices.

We consider a case where the double airfoil setup is acoustically compact, in which the acoustic wavelength is much larger than the airfoil's chord a and distance between them s. Noting that the acoustic wavelength equals $2\pi c_0/\omega$, compactness requires that sound dimensional frequency satisfies $\omega\ll 2\pi c_0/a$ and $\omega\ll 2\pi c_0/s$. When scaling the frequency by the convective unit U/a (as done in Section 2.3), this is equivalent to requiring $\overline{\omega}\ll 2\pi/M$ and $\overline{\omega}\ll 2\pi a/Ms$ for the non-dimensional frequency $\overline{\omega}$, where $M=U/c_0$ is the mean-flow Mach number. The first of the two conditions is satisfied automatically (as long as $\overline{\omega}\sim O(1)$) due to the small-Mach assumption set for using Eq. (13) [7,27]; yet, the second condition further requires that the airfoils are not too far apart, such that $Ms/a\ll 1$. From the physical point of view, the compact-setup approximation assumes that, to a leading order, the distance between each of the airfoils and the listener is identical and acoustic phase differences owing to different locations within the source zone are neglected.

In accordance with the assumption on system compactness, we apply the far-field two-dimensional form of the compact Green's function [7,27]:

$$G(\mathbf{x},\mathbf{y},t-\tau)\approx\frac{\mathbf{x}\cdot\mathbf{Y}}{2\pi\sqrt{2c_0|\mathbf{x}|^3}}\frac{\partial}{\partial t}\left\{\frac{H(t_r-\tau)}{\sqrt{t_r-\tau}}\right\},\quad |\mathbf{x}|\to\infty, \tag{19}$$

where $\mathbf{Y}(\mathbf{y})$ marks the *Kirchhoff* vector for the double-airfoil configuration, and $t_r=t-|\mathbf{x}|/c_0$ is the *acoustic retarded time*. The Kirchhoff vector $\mathbf{Y}(\mathbf{y})$ is given by

$$\mathbf{Y}(\mathbf{y})=\left(y_1,Y_2(y_1,y_2)\right), \tag{20}$$

where $Y_2(y_1,y_2)$, denoting the potential of uniform flow of unity magnitude in the y_2-direction over the two-airfoil system, is obtained numerically (see Appendix). Substitution of $G(\mathbf{x},\mathbf{y},t-\tau)$ into (16)–(18) yields explicit expressions for p_ξ, p_Γ and p_w.

Starting with the evaluation of $p_\xi(\mathbf{x},t)$, substitute (19) and (2) into (16). The time integration can be carried out explicitly, to yield

$$p_\xi^u(\mathbf{x},t)\approx-\frac{\overline{\varepsilon}\rho_0\omega^{5/2}\cos\theta}{4\sqrt{\pi c_0|\mathbf{x}|}}\left(\sin(\omega t_r)+\cos(\omega t_r)\right)\int_{-a}^{a}(y_1+a)\left(Y_2(y_1,s^+)-Y_2(y_1,s^-)\right)\mathrm{d}y_1,$$
$$p_\xi^l(\mathbf{x},t)\approx-\frac{\overline{\varepsilon}\rho_0\omega^{5/2}\cos\theta}{4\sqrt{\pi c_0|\mathbf{x}|}}\left[\cos\phi\left(\sin(\omega t_r)+\cos(\omega t_r)\right)+\sin\phi\left(\sin(\omega t_r)-\cos(\omega t_r)\right)\right]$$
$$\times\int_{-a}^{a}(y_1+a)\left(Y_2(y_1,-s^+)-Y_2(y_1,-s^-)\right)\mathrm{d}y_1, \tag{21}$$

for the separate contributions of upper and lower airfoil motions, respectively, and $p_\xi=p_\xi^u+p_\xi^l$. Here, $\cos\theta=x_2/|\mathbf{x}|$ indicates the observer direction, and $Y_2(y_1,\pm s^\pm)$ denotes values of the potential function Y_2 over the top and bottom surfaces of the airfoils.

To evaluate p_Γ, substitute (19) together with (14) into (17) to obtain

$$p_\Gamma(\mathbf{x},t)\approx\frac{\rho_0\Gamma\sin\theta}{2\pi\sqrt{2c_0|\mathbf{x}|}}\frac{\partial}{\partial t}\int_0^{t_r}\frac{V_\Gamma^{(2)}(\tau)\,\mathrm{d}\tau}{\sqrt{t_r-\tau}}$$
$$-\frac{\rho_0\Gamma\cos\theta}{2\pi\sqrt{2c_0|\mathbf{x}|}}\frac{\partial}{\partial t}\int_0^{t_r}\left(V_\Gamma^{(1)}(\tau)\frac{\partial Y_2}{\partial y_2}-V_\Gamma^{(2)}(\tau)\frac{\partial Y_2}{\partial y_1}\right)_{\mathbf{x}_\Gamma(\tau)}\frac{\mathrm{d}\tau}{\sqrt{t_r-\tau}}, \tag{22}$$

where $V_\Gamma^{(j)}$ denotes the velocity component of the incident vortex in the x_j-direction. Similarly, p_w is evaluated by substituting (19) and (14) into (18), to yield

$$p_w^u(\mathbf{x},t)\approx\sum_{k=1}^{n^u}\left(\frac{\rho_0\sin\theta}{2\pi\sqrt{2c_0|\mathbf{x}|}}\frac{\partial}{\partial t}\int_0^{t_r}\frac{\Gamma_k^u(\tau)V_{\Gamma_k^u}^{(2)}(\tau)\,\mathrm{d}\tau}{\sqrt{t_r-\tau}}\right.$$
$$\left.-\frac{\rho_0\cos\theta}{2\pi\sqrt{2c_0|\mathbf{x}|}}\frac{\partial}{\partial t}\int_0^{t_r}\Gamma_k^u(\tau)\left(V_{\Gamma_k^u}^{(1)}(\tau)\frac{\partial Y_2}{\partial y_2}-V_{\Gamma_k^u}^{(2)}(\tau)\frac{\partial Y_2}{\partial y_1}\right)_{\mathbf{x}_{\Gamma_k^u}(\tau)}\frac{\mathrm{d}\tau}{\sqrt{t_r-\tau}}\right),$$

$$p_w^l(\mathbf{x},t)\approx\sum_{k=1}^{n^l}\left(\frac{\rho_0\sin\theta}{2\pi\sqrt{2c_0|\mathbf{x}|}}\frac{\partial}{\partial t}\int_0^{t_r}\frac{\Gamma_k^l(\tau)V^{(2)}_{\Gamma_k^l}(\tau)\,\mathrm{d}\tau}{\sqrt{t_r-\tau}}\right.$$
$$\left.-\frac{\rho_0\cos\theta}{2\pi\sqrt{2c_0|\mathbf{x}|}}\frac{\partial}{\partial t}\int_0^{t_r}\Gamma_k^l(\tau)\left(V^{(1)}_{\Gamma_k^l}(\tau)\frac{\partial Y_2}{\partial y_2}-V^{(2)}_{\Gamma_k^l}(\tau)\frac{\partial Y_2}{\partial y_1}\right)_{\mathbf{x}_{\Gamma_k^l}(\tau)}\frac{\mathrm{d}\tau}{\sqrt{t_r-\tau}}\right),\tag{23}$$

for the separate contributions of upper and lower airfoil wakes, respectively, and $p_w=p_w^u+p_w^l$. Here, $V^{(j)}_{\Gamma_k^u}$ and $V^{(j)}_{\Gamma_k^l}$ mark the x_j-velocity component of the respective wake vortices.

Expressions (21)–(23) for the pressure components are calculated numerically, based on the near-field solution of the problem. Apart from the "lift-type" dipole found for p_ξ in (21) ($\propto\cos\theta$, therefore directed along the x_2-axis), both incident vortex and wake dipoles (22) and (23) have a "suction-type" component oriented along the mean-flow x_1-direction ($\propto\sin\theta$). In common with previous studies on single-airfoil noise [14–16], our calculations indicate that the suction pressure component is considerably smaller than the lift component at all times, and we therefore focus our results on studying the lift dipole contribution.

2.3. Scaling and numerical analysis

The problem formulated in Sections 2.1 and 2.2 is now scaled to obtain a non-dimensionalized problem. Normalizing the length, velocity, time, frequency and pressure by $a, U, a/U, U/a$ and ρ_0U^2, respectively, we find that the non-dimensional near-field problem is governed by

$$\overline{\varepsilon},\ \overline{\omega}=\frac{a}{U}\omega,\ \phi,\ \overline{s}=\frac{s}{a},\ \overline{\Gamma}=\frac{\Gamma}{2\pi aU}\text{ and }\overline{z}_{\Gamma_0}=\frac{z_{\Gamma_0}}{a},\tag{24}$$

specifying the scaled pitching amplitude and frequency, the phase-shift between airfoils' actuations, the separation distance between the airfoils, and the incident vortex circulation and initial location, respectively. To illustrate our results, we focus on a case where the incident vortex circulation is $\overline{\Gamma}=0.2$. The vortex is initially situated at $\overline{z}_{\Gamma_0}=-50+0.3\mathrm{i}$, sufficiently far upstream of the airfoils, where it essentially convects along a straight line with the mean flow. We study a case of relatively close airfoils, $\overline{s}=0.1$, to focus on the effects of mutual body and wake interactions on the flow-field and radiated sound. The pitching amplitude is taken as $\overline{\varepsilon}=0.01$, in accordance with the small-amplitude assumption set in Section 2.1. The pitching frequency is chosen to be $\overline{\omega}=1$, and the effect of phase shift angle ϕ is examined. Cases of pitching airfoils with steady flow ($\overline{\varepsilon}=0.01,\overline{\Gamma}=0$), and non-pitching airfoils in unsteady flow ($\overline{\varepsilon}=0,\overline{\Gamma}=0.2$) are studied separately and then combined. To assess the impact of double-airfoil interactions, our findings are compared to the results obtained in a counterpart single-airfoil setup.

The numerical solution of the dynamical problem is obtained using a discretization of the system of equations in both space (along airfoil's chords) and time (from $t=0$ to some final time). Space discretization is needed to express the vorticity distributions, $\overline{\gamma}_a^u(x_1,t)$ and $\overline{\gamma}_a^l(x_1,t)$, along the airfoils. The numerical solution for vorticity distributions is obtained via a standard Fourier-expansion procedure similar to the one described in Ref. [15] for a single airfoil. The system of equations is integrated in time using a fourth-order Runge–Kutta algorithm. The typical time step used for integration was $\Delta t=0.01$, which proved to be sufficient for convergence of the acoustic-field results (with errors <0.1 %).

Adopting the scaling introduced, the non-dimensional form of the acoustic pressure (15) becomes

$$\frac{p(\mathbf{x},t)}{\rho_0U^2}=\sqrt{\frac{M}{8|\overline{\mathbf{x}}|}}\Pi_{\mathrm{tot}}(\overline{t}_r)=\sqrt{\frac{M}{8|\overline{\mathbf{x}}|}}(\Pi_\xi(\overline{t}_r)+\Pi_\Gamma(\overline{t}_r)+\Pi_w(\overline{t}_r)),\tag{25}$$

where

$$\Pi_\xi(\overline{t}_r)=\Pi_\xi^u(\overline{t}_r)+\Pi_\xi^l(\overline{t}_r);$$
$$\Pi_\xi^u(\overline{t}_r)\approx-\frac{\overline{\varepsilon}\overline{\omega}^{5/2}\cos\theta}{\sqrt{2\pi}}\left(\sin(\overline{\omega}\overline{t}_r)+\cos(\overline{\omega}\overline{t}_r)\right)\int_{-1}^{1}(y_1+1)\left(\overline{Y}_2(y_1,\overline{s}^+)-\overline{Y}_2(y_1,\overline{s}^-)\right)\mathrm{d}y_1,$$
$$\Pi_\xi^l(\overline{t}_r)\approx-\frac{\overline{\varepsilon}\overline{\omega}^{5/2}\cos\theta}{\sqrt{2\pi}}\left[\cos\phi\left(\sin(\overline{\omega}\overline{t}_r)+\cos(\overline{\omega}\overline{t}_r)\right)+\sin\phi\left(\sin(\overline{\omega}\overline{t}_r)-\cos(\overline{\omega}\overline{t}_r)\right)\right]$$
$$\times\int_{-1}^{1}(y_1+1)\left(\overline{Y}_2(y_1,-\overline{s}^+)-\overline{Y}_2(y_1,-\overline{s}^-)\right)\mathrm{d}y_1,\tag{26}$$

$$\Pi_\Gamma(\overline{t}_r)\approx2\overline{\Gamma}\left[\sin\theta\frac{\partial}{\partial\overline{t}}\int_0^{\overline{t}_r}\frac{\overline{V}_\Gamma^{(2)}\,\mathrm{d}\tau}{\sqrt{\overline{t}_r-\tau}}-\cos\theta\frac{\partial}{\partial\overline{t}}\int_0^{\overline{t}_r}\left(\overline{V}_\Gamma^{(1)}\frac{\partial\overline{Y}_2}{\partial\overline{y}_2}-\overline{V}_\Gamma^{(2)}\frac{\partial\overline{Y}_2}{\partial\overline{y}_1}\right)_{\overline{\mathbf{x}}_{\overline{\Gamma}}(\tau)}\frac{\mathrm{d}\tau}{\sqrt{\overline{t}_r-\tau}}\right],\tag{27}$$

and

$$\Pi_w(\overline{t}_r)=\Pi_w^u(\overline{t}_r)+\Pi_w^l(\overline{t}_r);$$

$$\Pi_w^u(\bar{t}_r) \approx 2\sum_{k=1}^{n^u}\left[\sin\theta\frac{\partial}{\partial\bar{t}}\int_0^{\bar{t}_r}\frac{\overline{\Gamma}_k^u\overline{V}_{\Gamma_k^u}^{(2)}\,\mathrm{d}\tau}{\sqrt{\bar{t}_r-\tau}} - \cos\theta\frac{\partial}{\partial\bar{t}}\int_0^{\bar{t}_r}\overline{\Gamma}_k^u\left(\overline{V}_{\Gamma_k^u}^{(1)}\frac{\partial\overline{Y}_2}{\partial\overline{y}_2} - \overline{V}_{\Gamma_k^u}^{(2)}\frac{\partial\overline{Y}_2}{\partial\overline{y}_1}\right)_{\overline{\mathbf{x}}_{\Gamma_k^u}(\tau)}\frac{\mathrm{d}\tau}{\sqrt{\bar{t}_r-\tau}}\right],$$

$$\Pi_w^l(\bar{t}_r) \approx 2\sum_{k=1}^{n^l}\left[\sin\theta\frac{\partial}{\partial\bar{t}}\int_0^{\bar{t}_r}\frac{\overline{\Gamma}_k^l\overline{V}_{\Gamma_k^l}^{(2)}\,\mathrm{d}\tau}{\sqrt{\bar{t}_r-\tau}} - \cos\theta\frac{\partial}{\partial\bar{t}}\int_0^{\bar{t}_r}\overline{\Gamma}_k^l\left(\overline{V}_{\Gamma_k^l}^{(1)}\frac{\partial\overline{Y}_2}{\partial\overline{y}_2} - \overline{V}_{\Gamma_k^l}^{(2)}\frac{\partial\overline{Y}_2}{\partial\overline{y}_1}\right)_{\overline{\mathbf{x}}_{\Gamma_k^l}(\tau)}\frac{\mathrm{d}\tau}{\sqrt{\bar{t}_r-\tau}}\right]. \tag{28}$$

In (28), $\overline{\Gamma}_k^u = \Gamma_k^u/(2\pi aU)$ and $\overline{\Gamma}_k^l = \Gamma_k^l/(2\pi aU)$.

Results for the acoustic pressure are presented in terms of the acoustic "kernels" defined in (25)–(28). In addition to the parameters introduced in Eq. (24), the non-dimensional acoustic pressure is governed by the observer direction, $\theta = \cos^{-1}(x_2/|\mathbf{x}|)$.

3. Results

3.1. Pitching airfoils at steady flow

We begin by considering the case of pitching airfoils at steady flow, i.e. in the absence of an incident vortex ($\overline{\Gamma}=0$). Disregarding transient effects obtained at times close to the initial time of actuation ($\bar{t}=0$), we focus on analyzing the time-periodic behavior of the system achieved at $\bar{t}\gg 1$. To study the impact of phase angle ϕ between airfoils' actuations on system acoustic properties, we compare cases of in-phase ($\phi=0$) and counter-phase ($\phi=\pi$) forcing (see Eq. (1)).

Fig. 2 presents the long-time acoustic radiation of the system. The solid lines in Fig. 2a and b show the separate contributions of airfoils' motion and system wake to the acoustic field in an in-phase ($\phi=0$) actuation, respectively, and the

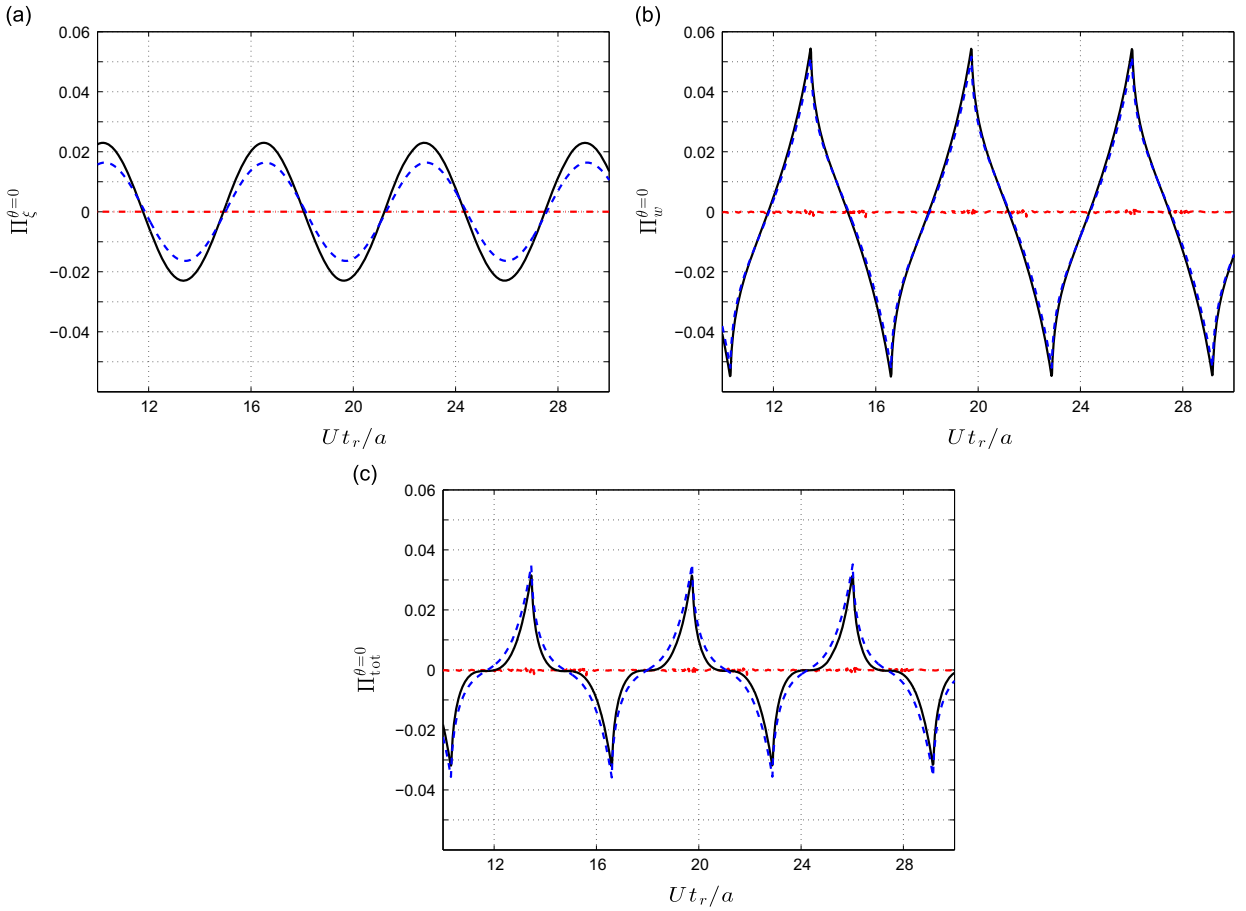

Fig. 2. Acoustic radiation of pitching ($\overline{e}=0.01, \overline{\omega}=1$) side-by-side airfoils at steady flow ($\overline{\Gamma}=0$): components of (a) airfoils' motion and (b) wake sound radiations in the normal ($\theta=0$) direction; (c) total sound radiation in the normal ($\theta=0$) direction. In all figures, solid and red dash-dotted lines present data for in-phase ($\phi=0$) and counter-phase ($\phi=\pi$) pitching airfoils, respectively. Dashed blue lines mark results for a counterpart single airfoil setup. (For interpretation of the references to color in this figure caption, the reader is referred to the web version of this paper.)

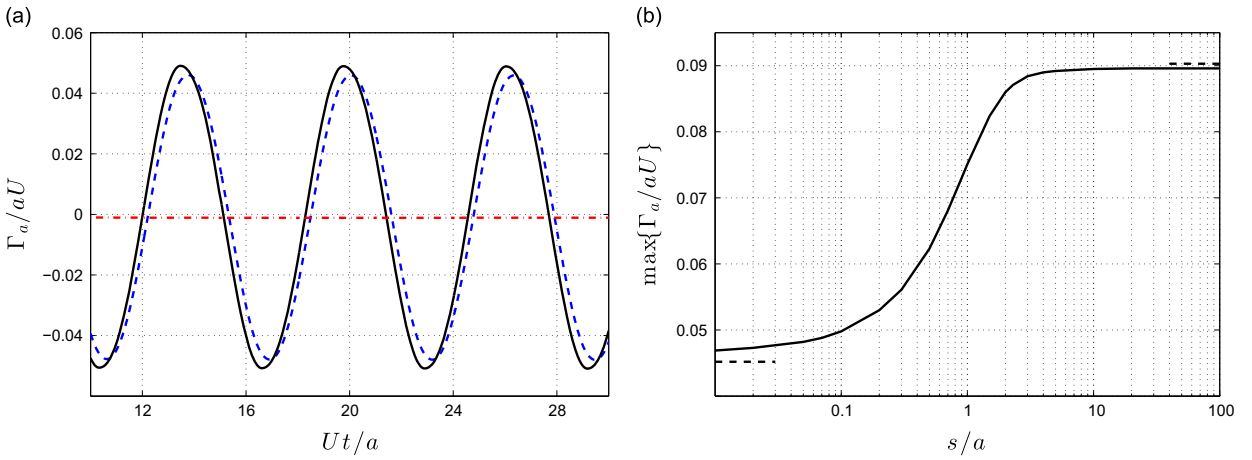

Fig. 3. Near-field characteristics of the motion of pitching ($\overline{\varepsilon}=0.01, \overline{\omega}=1$) side-by-side airfoils at steady flow ($\overline{\Gamma}=0$): (a) Sum of time variations of airfoil circulations, $\overline{\Gamma}_a=\overline{\Gamma}^u_a+\overline{\Gamma}^l_a$, for airfoils located $s/a=0.1$ apart; solid and red dash-dotted lines mark data for in-phase ($\phi=0$) and counter-phase ($\phi=\pi$) pitching airfoils, respectively, and dashed blue line marks counterpart result for a single airfoil. (b) Effect of the airfoils' separation parameter, s/a, on the maximum magnitude of $\overline{\Gamma}_a=\overline{\Gamma}^u_a+\overline{\Gamma}^l_a$ in an in-phase ($\phi=0$) pitching setup. Short dashed horizontal lines mark asymptotic values of maximum total circulation at small and large values of the distance parameter. (For interpretation of the references to color in this figure caption, the reader is referred to the web version of this paper.)

solid line in Fig. 2c gives the corresponding total radiation. Dash-dotted lines show counterpart results for airfoils in counter-phase ($\phi=\pi$) actuation, and dashed lines present data in the case of a single airfoil pitching at the same frequency, for reference.

Comparing between the results for in-phase and counter-phase airfoils, we observe that radiation in the counter-phase case is vanishingly small compared with the $\phi=0$ case. For the airfoils'-motion component Π_ξ, this can be easily rationalized through the explicit expressions appearing in Eq. (26). Specifically, when considering the symmetry properties of the velocity potential $Y_2(y_1,y_2)$ (see Appendix), we find that the separate contributions of upper and lower airfoils' sound, Π^u_ξ and Π^l_ξ in (26), are equal for $\phi=0$ and opposite in sign for $\phi=\pi$. This, in turn, leads to the vanishing dash-dotted contribution in Fig. 2a in the counter-phase case. The counter-phase cloaking mechanism may be of practical importance, particularly at large actuation frequencies: noting the $\overline{\omega}^{5/2}$ power dependence of Π_ξ in (26), our calculations show that the total sound radiation is dominated by Π_ξ for $\phi=0$ when $\overline{\omega}\gg 1$. Yet, in the counter-phase $\phi=\pi$ case, or in its vicinity, this contribution (being $O(\overline{\omega})^{5/2}$ for Π^u_ξ and Π^l_ξ separately) vanishes.

Turning to the wake-noise component presented in Fig. 2b, we note that a similar mechanism of sound attenuation is observed. Here, our calculations indicate that the wake in the in-phase case is composed of two in-phase wakes released from the airfoils, each of which consists of a vortex street of vortices of equal strength and alternating signs. Having identical in-phase properties (see the discussion in Fig. 3), the two identical wakes contribute equally to the total wake sound. Yet, in the counter-phase ($\phi=\pi$) case, the two wakes approximately cancel each other, leading to the nearly vanishing signal shown by the dash-dotted line in Fig. 2b.

Comparing the two-airfoil and single-airfoil acoustic signatures presented in Fig. 2, we observe that single-airfoil radiation is similar to the signature of the in-phase system. It is therefore concluded that for the present choice of relatively close airfoils (with a separation distance of $s/a=0.1$), the in-phase airfoil–fluid interaction is acoustically equivalent to the single pitching airfoil setup. Particular similarity is shown by the almost identical wake noise signals obtained in the single-airfoil (dashed line in Fig. 2b) and in-phase airfoils (solid line in Fig. 2b, which is the sum of equal upper and lower airfoils wake contributions) setups. For the direct airfoil-motion noise, the results in Fig. 2a show small differences, with the double-airfoil setup being slightly noisier. In both cases, wake noise and direct airfoil noise act to cancel each other, leading to the total signal shown in Fig. 2c. Here, the single-airfoil system is found slightly noisier than the double-airfoil configuration.

To gain further insight into the findings of Fig. 2, Fig. 3 presents comparison between near-field flow characteristics of the side-by-side and single pitching airfoils at steady flow conditions, as in Fig. 2. To this end, we introduce the total circulations of each of the airfoils in the double-airfoil setup:

$$\overline{\Gamma}^u_a=\int_{-1}^{1}\overline{\gamma}^u_a(x_1,\overline{t})\,dx_1 \quad \text{and} \quad \overline{\Gamma}^l_a=\int_{-1}^{1}\overline{\gamma}^l_a(x_1,\overline{t})\,dx_1, \tag{29}$$

and calculate the total system circulation, $\overline{\Gamma}_a=\overline{\Gamma}^u_a+\overline{\Gamma}^l_a$. In Fig. 3a, the latter is compared with total airfoil circulation in a single airfoil case. In Fig. 3b, the variation of the maximum value of $\overline{\Gamma}_a$ with the normalized distance between the airfoils, s/a ($=0.1$ in Figs. 2 and 3a), in an in-phase pitching setup, is presented.

In line with the findings in Fig. 2, Fig. 3a shows that the single-airfoil and in-phase pitching airfoil circulations are closely correlated. In addition, the total circulation in the counter-phase setup is vanishingly small, reflecting the sum of opposite-sign

circulations of the upper and lower airfoils. While the latter result for counter-phase airfoils remains unchanged when varying the distance between the airfoils, changes in the total system circulation with varying s/a are observed in the in-phase actuation setup, as shown in Fig. 3b. Thus, when the distance between the airfoils increases above $s/a \approx 10$, their mutual effects vanish, and they may be considered as two separate airfoils. Consequently, the total system circulation is given by the sum of two single airfoils immersed in an unbounded domain. The dashed line in the upper right part of Fig. 3b depicts the respective asymptotic value of ≈ 0.09, being the double of the maximum value of single airfoil circulation (given by the maxima in the dashed line in Fig. 3a). In the other limit, when the airfoils are closely situated ($s/a \ll 1$), their wakes closely interact and they effectively act as a single airfoil. The limit value of maximum system circulation is then ≈ 0.045, as presented by the dashed line in the lower left part of Fig. 3b. This value is only approximately achieved by our calculations, owing to numerical limitations of the numerical scheme occurring when airfoil's trailing edges become excessively adjacent.

3.2. Non-pitching airfoils at unsteady flow

To study the separate effects of flow unsteadiness on system acoustic radiation, Fig. 4 presents the acoustic signature of non-pitching ($\overline{\varepsilon} = 0$) side-by-side airfoils for unsteady flow conditions ($\overline{\Gamma} = 0.2$). Separate components of incident vortex and wake sound are presented by the solid lines in Fig. 4a and b, respectively, and the total signature is given by the solid line in Fig. 4c. As in the preceding section, the results are compared with counterpart data for a single-airfoil setup subject to identical flow conditions, as described by the dashed lines. Fig. 4d shows the total sound energy for the double- and single-airfoil systems, defined by integration of the squared total radiation of each of the systems over a circle of radius

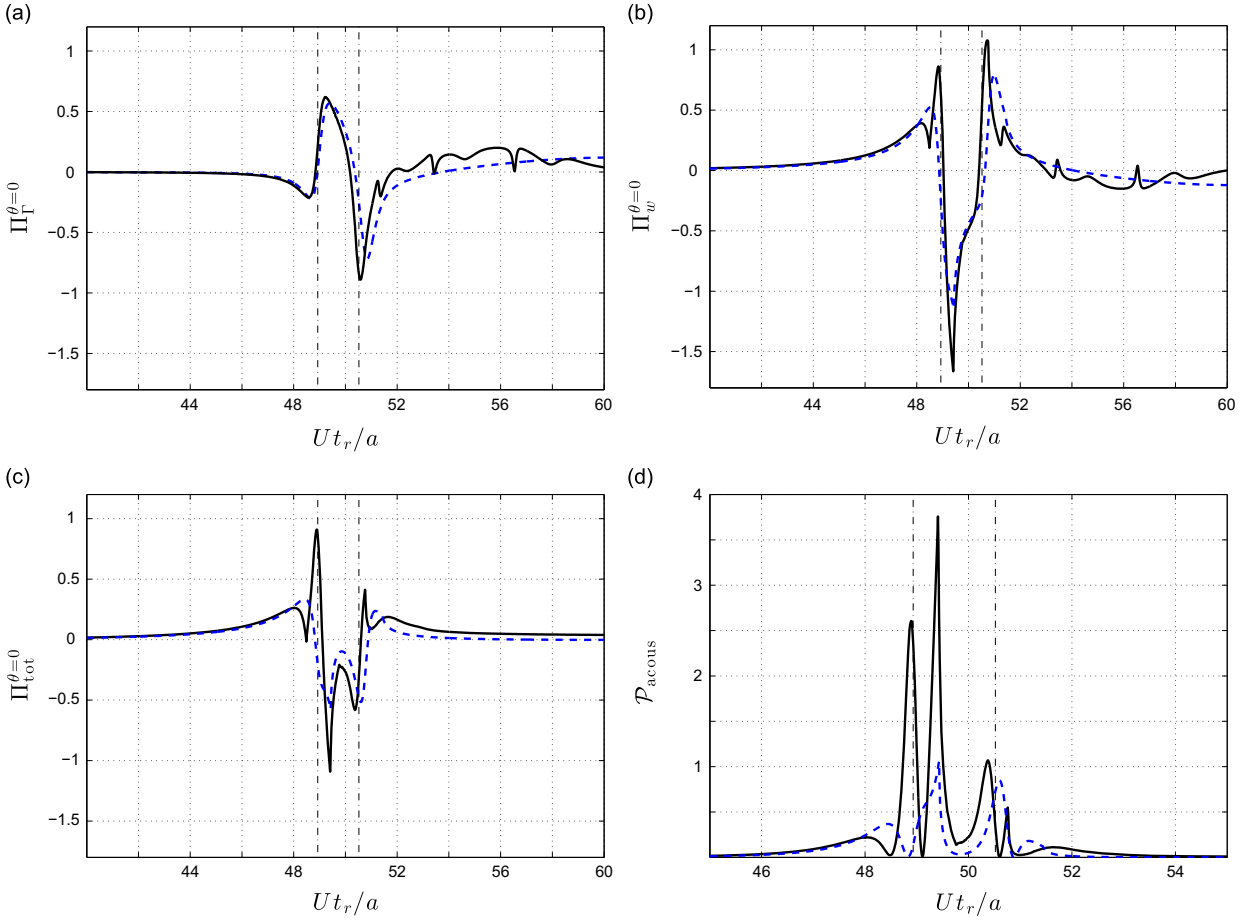

Fig. 4. Acoustic radiation of non-pitching ($\overline{\varepsilon} = 0$) side-by-side airfoils for unsteady flow ($\overline{\Gamma} = 0.2$): components of (a) incident vortex and (b) wake sound radiations in the normal ($\theta = 0$) direction (solid lines); (c) total sound radiation in the normal ($\theta = 0$) direction (solid line); (d) total sound energy (solid line). In all figures, dashed blue lines mark data for a single-airfoil setup. Dash-dotted vertical lines confine the time interval during which the vortex passes above the double-airfoil configuration. (For interpretation of the references to color in this figure caption, the reader is referred to the web version of this paper.)

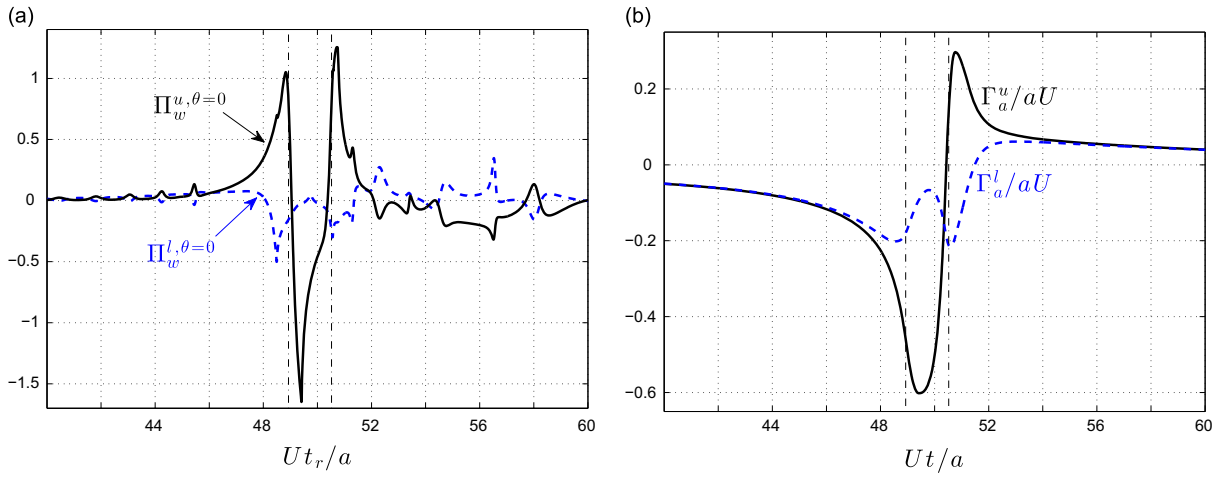

Fig. 5. Separate effects of upper and lower airfoils on far- and near-flow-field characteristics of non-pitching airfoils ($\bar{\varepsilon}=0$) for unsteady flow ($\bar{\Gamma}=0.2$): (a) separate contributions of upper (solid line) and lower (dashed line) airfoil wakes to total wake noise in the normal ($\theta=0$) direction; (b) time variations of upper (solid line) and lower (dashed line) airfoil circulations. Vertical dash-dotted lines confine the time interval during which the vortex passes above the airfoils.

$|\overline{\mathbf{x}}|\to\infty$:

$$\mathcal{P}_{\text{acous}}(\bar{t}_r)=\int_0^{2\pi}\Pi_{\text{tot}}^2(\bar{t}_r,\theta)\,\mathrm{d}\theta. \tag{30}$$

The dash-dotted vertical lines in each figure confine the time interval during which the incident vortex passes above the double-airfoil configuration. This time interval remains nearly unchanged between the single- and double-airfoil configurations.

Focusing on the total signature and sound energy of the systems in Fig. 4c and d, we find that the double-airfoil setup is generally noisier than the single-airfoil system. While this may have been expected due to the interaction of vorticity with multiple sharp edges in the case of double-airfoil setup, it is not uniformly valid at all times. Thus, there exist time intervals, particularly in the vicinity of leading-edge and trailing-edge times (i.e., when the incident vortex passes above $\bar{x}_1=\pm 1$), where the single-airfoil system radiates more sound. Inspection of Fig. 4a and b indicates that these time-intervals of sound reduction are attributed to the wake sound component, being attenuated close to leading and trailing edge times compared with the single-airfoil setup.

To investigate the latter observation, Fig. 5 examines the separate contributions of upper and lower airfoils to total system wake noise (Fig. 5a) and total circulation (Fig. 5b). Remarkably, as the incident vortex approaches the airfoils and passes above them, the wake released by the lower airfoil radiates sound which acts to reduce the noise generated by the upper airfoil wake (note the opposite signs of Π_w^u and Π_w^l in Fig. 5a). In terms of near-field characteristics, the reason for that is clarified in Fig. 5b. As the incident vortex approaches the airfoils' leading edges, the lower airfoil circulation (which, at earlier times, is identical with upper airfoil circulation) starts deviating from the upper airfoil circulation gradually (see the differences between the curves in Fig. 5b, beginning at $\bar{t}\approx 47$). Recalling that, according to the Kelvin theorem, time variations of airfoils' circulations reflect time variations of the total wake circulations (see Eqs. (10) and (29)), this deviation reflects the shedding of wake vortices from the lower trailing edge that are opposite in sign to those released at the upper trailing edge. This opposite-sign vorticity release, which results from the nonlinear interaction between the two wakes and the incoming vortex, leads to the noise reduction effect observed in Fig. 5a. The mechanism is most effective at leading and trailing edge times, and therefore only then the total system radiation may become lower than radiation by a single airfoil. At late times, both airfoils' circulations become equal again, and vanish to their vanishing unperturbed value.

3.3. Combined forcing

Having studied the separate effects of pitching and flow unsteadiness on system acoustic properties, Fig. 6 presents the total acoustic radiation from side-by-side airfoils subject to both incident vortex loading and leading edge animation. Both parts of the figure show the total radiation in the lift ($\theta=0$) direction, but focus on different time intervals, for clarity of presentation (note the difference in the Π_{tot}-axis scale between the two figures).

Starting with a time interval prior to vortex passage above the airfoil, Fig. 6a shows a comparison between the acoustic radiation of in-phase (solid line), counter-phase (dash-dotted line) and single (dashed line) airfoil setups for $25\le\bar{t}_r\le 40$. During this time interval, when the impact of incoming vorticity is relatively small, the total radiations appear similar in form to the steady-flow signatures discussed in Section 3.1. Specifically, the signature of the in-phase setup is qualitatively similar to the single-airfoil radiation, while the sound level calculated in the counter-phase case is considerably smaller.

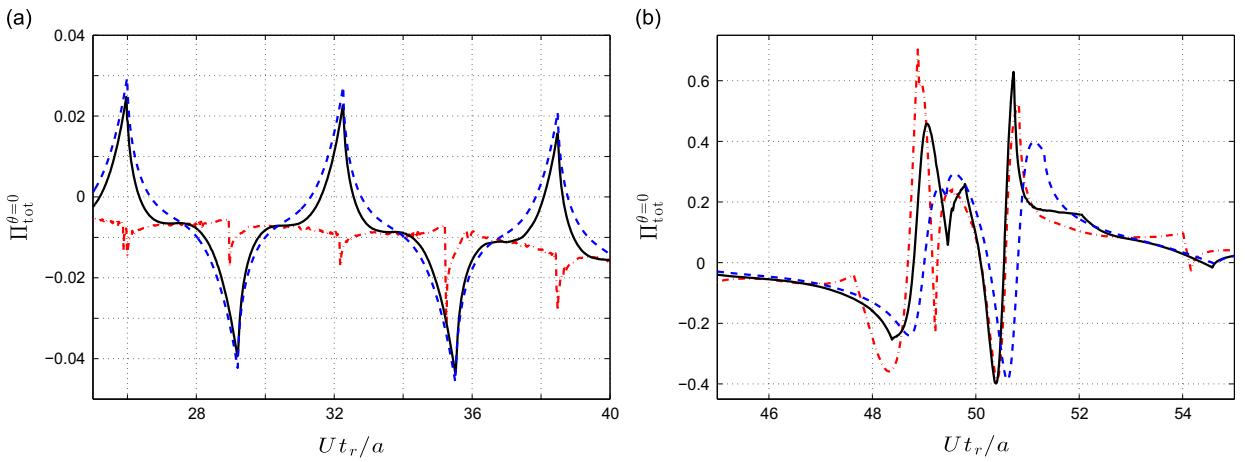

Fig. 6. Total acoustic radiation in the normal ($\theta=0$) direction for pitching ($\overline{\varepsilon}=0.01, \overline{\omega}=1$) side-by-side airfoils subject to incident vortex ($\overline{\Gamma}=0.2$) loading. (a) and (b) present the total radiation at different time intervals. Solid and red dash-dotted lines show data for in-phase ($\phi=0$) and counter-phase ($\phi=\pi$) pitching airfoils, respectively. Dashed blue lines mark data for a single pitching airfoil. (For interpretation of the references to color in this figure caption, the reader is referred to the web version of this paper.)

Yet, unlike the steady-flow result in Fig. 2c, the counter-phase setup generates non-negligible sound owing to finite interaction with the incoming vortex.

The comparison changes qualitatively during the time interval when the vortex passes above the airfoils, as depicted in Fig. 6b.[2] Here, the counter-phase pitching setup becomes considerably noisier than at earlier times, and similar in magnitude to the in-phase configuration. Both setups are generally noisier than the single-airfoil system, excluding time-intervals close to leading- and trailing-edge times, in accordance with the wake sound-reduction mechanism discussed in Section 3.2. Interestingly, it is observed that the counter-phase system generates the highest sound level at leading edge time. Our calculations indicate that this result is dependent on the specific time in which the vortex interacts with the airfoils end points, in terms of the airfoils' pitching period. Thus, we find that varying the vortex initial location (i.e., so that the vortex reaches the airfoils at a different time phase along their pitching period) results in quantitatively different ratios between sound levels in in-phase and counter-phase systems. Detailed study of the effect of vortex initial location on the results in Fig. 6b (which is also equivalent to varying the phase difference ϕ between airfoils' pitching actuations) is skipped here for brevity.

4. Conclusion

We examined the acoustic radiation of a side-by-side airfoil configuration, subject to small-amplitude harmonic pitching animation and unsteady flow conditions. The two-dimensional near-field problem was analyzed using thin-airfoil theory, where flow unsteadiness was modeled in the form of a passing line vortex, and wake evolution was calculated using the Brown and Michael formula. Assuming that the setup is acoustically compact, acoustic radiation was calculated using the Powell–Howe acoustic analogy, where the compact Green's function was calculated numerically using potential-flow analysis of the flow-field. Our results, comparing the acoustic radiation of the double-airfoil system to a reference case of a single airfoil, indicate several mechanisms of sound attenuation and sound amplification caused by airfoil–airfoil and airfoil–wake interactions. For the problem in the absence of incoming flow vorticity, it is found that counter-phase pitching of the airfoils results in effective acoustic cloaking of the system, which otherwise becomes dominated by direct pitching-motion sound (which increases like 5/2-power of the pitching frequency). In addition, depending on distance between airfoils, in-phase pitching may result in an acoustic signature equivalent to a single airfoil (when the airfoils are adjacent) or to two separate airfoils (when the airfoils are far apart). Flow unsteadiness generally produces more sound in the proximity of the double-airfoil setup. Yet, airfoils' nonlinear wake–wake interactions lead to a sound reduction mechanism, most efficient at times when incoming vorticity passes above airfoil's leading and trailing edges.

The present analysis relies strongly on the assumption of acoustic compactness, by neglecting acoustic-phase differences within the source zone compared with the wavelength of far-field acoustic radiation. Thus, apart from confining validity of our findings to relatively low frequencies ($\overline{\omega}\ll 2\pi/M$, with $\overline{\omega}$ being normalized by airfoil-chord-based scale, and M being the mean flow Mach number), compactness also requires that $M\overline{s}\ll 1$, where $\overline{s}$ measures the scaled distance between the airfoils (see Section 2.2). To the extent that these restrictions are satisfied, our scheme can be easily extended to consider the acoustic properties of other double-airfoil configurations (apart from side-by-side setup), as well as multiple (>2)

[2] The time interval of vortex passage above the airfoils is not marked in Fig. 6b for clarity, as it slightly varies between configurations. Yet, it is roughly between $49\lesssim\overline{t}_r\lesssim 50.7$ in all cases.

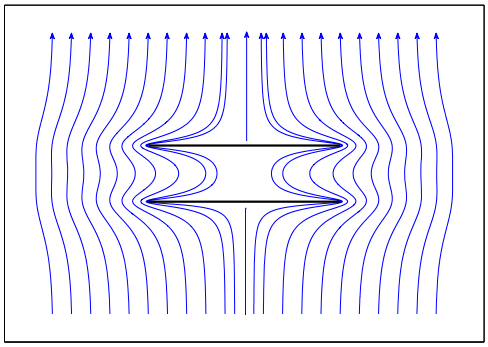

Fig. 7. Streamlines of the potential flow field $Y_2(y_1, y_2)$.

airfoils' setups. A desirable, though less immediate, extension of the present work would include the effect of structural elasticity (replacing presently assumed rigid airfoil) on the system acoustic properties.

Acknowledgements

This research was supported by the Marie Curie International Reintegration Grant no. PIRG-GA-2010-276837 and by the J. and J. Gringorten Aeronautical Research Fund.

Appendix A. Calculation of $Y_2(y_1, y_2)$

Evaluation of $Y_2(y_1, y_2)$, the velocity potential of uniform unit flow in the y_2-direction over the airfoils, is carried out numerically via a finite-difference solution of Laplace's equation. The equation is solved in conjunction with impermeability conditions on the airfoils, using a MATLAB subroutine. For actual calculation, airfoils of finite width must be considered. To comply with our thin-airfoil assumption, we considered a case where the ratio between airfoil's thickness and chord is 10^{-3}, and verified that further decrease in airfoil's thickness does not affect the numerical results. In addition, it has been verified that the numerical calculation captures the close-form solution for $Y_2(y_1, y_2)$ for a single airfoil [27]. Note that a solution for $Y_2(y_1, y_2)$ may also be obtained using the Sedov method [28], which gives a general formula for the potential of uniform flow over an arbitrary set of parallel airfoils. Yet, since an explicit application of Sedov's formula in the present case requires numerical analysis of a complex-variable integral, we have preferred the present methodology owing to its relative simplicity.

Fig. 7 shows a characteristic plot of the flow streamlines obtained from the numerical solution. At large distances from the airfoils, the flow is directed uniformly along the y_2 vertical axis. The calculated flow field is symmetric about the $y_1 = 0$ and $y_2 = 0$ mid-plane axes.

References

[1] M.M. Zdravkovich, Review of flow interference between two circular cylinders in various arrangements, *Journal of Fluids Engineering* 99 (1977) 618–633.
[2] J.C. Liao, D.N. Beal, G.V. Lauder, M.S. Triantafyllou, Fish exploiting vortices decrease muscle activity, *Science* 302 (2003) 1566–1569.
[3] L. Zannetti, F. Gallizio, G.M. Ottino, Vortex motion in doubly connected domains, *Journal of Fluid Mechanics* 612 (2008) 143–152.
[4] H. Aziz, R. Mukherjee, Unsteady aerodynamics of multiple airfoils in configuration, *International Journal of Advances Computer Science* 2 (2012) 399–411.
[5] S.F. Harding, I.G. Bryden, Generating controllable velocity fluctuations using twin oscillating hydrofoils, *Journal of Fluid Mechanics* 713 (2012) 150–158.
[6] Y. Bao, J.J. Tao, Dynamic reactions of a free-pitching foil to the reverse Kármán vortices, *Physics of Fluids* 26 (2014) 031704.
[7] M.S. Howe, *Acoustics of Fluid–Structure Interactions*, Cambridge University Press, Cambridge, 1998.
[8] O. Inoue, M. Mori, N. Hatakeyama, Aeolian tones radiated from flow past two square cylinders in tandem, *Physics of Fluids* 18 (2006) 046101.
[9] C.J. Doolan, Flow and Noise simulation of the NASA tandem cylinder experiment using openFOAM, AIAA Paper (2009) AIAA-2009-3157.
[10] D. Casalino, M. Jacob, M. Roger, Prediction of rod–airfoil interaction noise using the Ffowcs–Williams–Hawkings analogy, *AIAA Journal* 41 (2003) 182–191.
[11] D.J.J. Leclercq, C.J. Doolan, The interaction of a bluff body with a vortex wake, *Journal of Fluids and Structures* 25 (2009) 867–888.
[12] J. Winkler, T. Carolus, Trailing-edge blowing on tandem airfoils: aerodynamic and aeroacoustic implications, AIAA Paper (2010) AIAA-2010-3981.
[13] M. Gruber, P.F. Joseph, C. Polacsek, T. P. Chong, Noise reduction using combined trailing edge and leadingedge serrations in a tandem airfoil experiment, AIAA Paper (2012) AIAA-2012-2134.
[14] A. Manela, Nonlinear effects of flow unsteadiness on the acoustic radiation of a heaving airfoil, *Journal of Sound and Vibration* 332 (2013) 7076–7088.
[15] A. Manela, L. Huang, Point vortex model for prediction of sound generated by a wing with flap interacting with a passing vortex, *Journal of the Acoustical Society of America* 133 (2013) 1934–1944.
[16] A. Manela, On the acoustic radiation of a pitching airfoil, *Physics of Fluids* 25 (2013) 071906.
[17] C.E. Brown, W.H. Michael, Effect of leading edge separation on the lift of a delta wing, *Journal of the Aeronautical Sciences* 21 (1954) 690–706.
[18] C.E. Brown, W.H. Michael, On Slender Delta Wings with Leading-edge Separation. NACA Technical Note 3430, 1955.
[19] S. Michelin, S.G. Llewellyn Smith, B.J. Glover, Vortex shedding model of a flapping flag, *Journal of Fluid Mechanics* 617 (2008) 1–10.
[20] S. Michelin, S.G. Llewellyn Smith, Resonance and propulsion performance of a heaving flexible wing, *Physics of Fluids* 21 (2009) 071902.
[21] S. Michelin, S.G. Llewellyn Smith, An unsteady point vortex method for coupled fluid–solid problems, *Theoretical and Computational Fluid Dynamics* 23 (2009) 127–153.

[22] X. Dai, X. Jing, X. Sun, Vortex shedding and its nonlinear acoustic effect occurring at a slit, *AIAA Journal* 49 (2011) 2684–2694.
[23] X. Dai, X. Jing, X. Sun, Discrete vortex model of a Helmholtz resonator subjected to high-intensity sound and grazing flow, *Journal of the Acoustical Society of America* 132 (2012) 2988–2996.
[24] H. Glauert, *The Elements of Aerofoil and Airscrew Theory*, Cambridge University Press, Cambridge, 1959.
[25] M.C.A.M. Peters, A. Hirschberg, Acoustically induced periodic vortex shedding at sharp edged open channel ends: *simple vortex models*, *Journal of Sound and Vibration* 161 (1993) 281–299.
[26] M.S. Howe, Emendation of the Brown & Michael equation, with application to sound generation by vortex motion near a half-plane, *Journal of Fluid Mechanics* 329 (1996) 89–101.
[27] M.S. Howe, *Theory of Vortex Sound*, Cambridge University Press, Cambridge, 2003.
[28] M.S. Howe, *Hydrodynamics and Sound*, Cambridge University Press, Cambridge, 2006.